AIAA JOURNAL
Vol. 61, No. 12, December 2023

Numerical Study of Circular-Cylinder Disturbance Generators with Rigid Splitter Plates

Michael Jenkins*
North Carolina State University, Raleigh, North Carolina 27695
Arun Vishnu Suresh Babu†
University of North Carolina at Charlotte, Charlotte, North Carolina 28223
and
Matthew Bryant‡ and Ashok Gopalarathnam§
North Carolina State University, Raleigh, North Carolina 27695

https://doi.org/10.2514/1.J062729

This paper describes the numerical study of oscillating circular cylinders with rigid splitter plates of different lengths. These geometries may be used as disturbance generators for the study of unsteady airfoils and wings operating in highly vortical flowfields. It has been shown that cylinders undergoing forced rotational oscillations at their natural shedding frequency can produce wakes with minimal deviation in cycle-to-cycle vortex strength and position. Adding a splitter plate allows these deviations to be reduced even further. We present cases for oscillating cylinders having splitter-plate lengths up to 1.25d at a Reynolds number of 7600. Frequencies are maintained at the natural shedding frequency, and a rotational amplitude of 45 deg is used. Numerical simulations are performed using a two-dimensional unsteady Reynolds-averaged Navier–Stokes (RANS) code. Results are presented in the form of vorticity contours and cycle-averaged velocity profiles, as well as the dominant frequencies of cylinder lift force and downstream velocity angles. The results show that splitter-plate lengths shorter than 0.5d adversely affect the ability to generate a coherent vortex wake due to shear layer roll-up near the trailing edge of the plate. Splitter plates longer than 0.75d produced a reverse von Kármán wake with consistent cycle-to-cycle vortex shedding.

Nomenclature

A	=	area of integration for circulation, m^2
C_D	=	drag coefficient
C_L	=	lift coefficient
C_M	=	pitching moment coefficient
$C_{L,\mathrm{RMS}}$	=	root mean square of lift coefficient
d	=	cylinder diameter, m
F_D	=	drag force, N
F_L	=	lift force, N
f	=	frequency, Hz
f_n	=	natural shedding frequency, Hz
f_{osc}	=	oscillation frequency, Hz
ℓ	=	splitter plate length, m
M	=	pitching moment about the cylinder, N · m
St	=	Strouhal number
T	=	cycle time, s
t	=	physical time, s
t^*	=	nondimensional time step, tU_∞/d
U_T	=	tangential cylinder velocity, m/s
U_∞	=	freestream reference velocity, m/s
u, v	=	velocity components, m/s
x, y	=	Cartesian coordinates, m
y^+	=	nondimensional wall distance
Γ	=	circulation, m^2/s
θ	=	rotation angle, deg
θ_A	=	maximum oscillation amplitude, deg
ρ	=	reference fluid density, kg/m^3
ω	=	vorticity, 1/s

Presented as Paper 2022-3991 at the 2022 AIAA Aviation Forum, Chicago, IL, June 27–July 1, 2022; received 13 December 2022; revision received 7 August 2023; accepted for publication 9 August 2023; published online 31 October 2023.

*Ph.D. Student, Department of Mechanical and Aerospace Engineering; mgjenkin@ncsu.edu.
†Teaching Assistant Professor, Department of Mechanical Engineering and Engineering Science; asures10@uncc.edu.
‡Associate Professor, Department of Mechanical and Aerospace Engineering; mbryant@ncsu.edu.
§Professor, Department of Mechanical and Aerospace Engineering; agopalar@ncsu.edu. Associate Fellow AIAA.

I. Introduction

THE behavior of unsteady airfoils and wings in the presence of external flow disturbances is a topic of growing importance as it relates to many applications, such as formation flight, aerial refueling, wind turbine arrays, and energy harvesting, to name a few. External disturbances are known to modify the aerodynamic and aeroelastic behavior of wings [1–6]. The systematic study of disturbance encounters requires controlled generation of flow disturbances that can be timed with respect to the kinematic profile of the wings. Recent research by Rockwood and Medina [7] showed that a rotating circular cylinder with an attached splitter plate of one-diameter length is a promising systematic disturbance generation mechanism that provides the ability to control the frequency and strength of the vortical wakes as well as to synchronize the disturbances with the motion of a downstream wing. In this paper we explore circular-cylinder-based disturbance-generators with various plate lengths in comparison to stationary and rotationally oscillating circular cylinders. We present a detailed characterization of the geometries from a fluid dynamics perspective to reveal the effect of varying the plate length on the vortex formation and shedding pattern as well as from a mechanical design perspective to identify the aerodynamic loads experienced by the disturbance generators.

Vortex-dominated wakes behind various bluff-body geometries, including circular [8,9], rectangular [10], square [11], and elliptical [12] cylinders, have been explored thoroughly in the literature. It is well known that a stationary circular cylinder exhibits the classical von Kármán vortex street and that the Strouhal number, representing the fundamental vortex shedding frequency, depends primarily on the Reynolds number. It is also known that the vortex shedding results in a drag producing wake, and the drag oscillates at twice the natural vortex shedding frequency, whereas the fluctuating lift exhibits the same frequency as the vortex shedding frequency. The vortical structures in the wake cause velocity and flow-angle fluctuations in

the flowfield, and hence can be used to emulate gust encounters on downstream wings. Liao et al. [13] used a stationary circular cylinder to study vortex interactions on a downstream airfoil and found that the lift and vortex shedding frequency of the airfoil would synchronize with the natural shedding frequency of the cylinder. Because the vortex shedding frequency and pattern of a stationary cylinder are fixed for given flow conditions, the ability to vary the intensity of the oncoming disturbances or their phase relative to the motion of a downstream wing is limited. Translational and rotational motions can alter the boundary-layer interaction and vortex formation in circular cylinders [14] and hence may be used as a mechanism to tailor the wake characteristics. Forced cylinder oscillation has been investigated using both experimental and numerical techniques [15–19]. In a recent study by Suresh Babu et al. [20], sinusoidal rotation of a circular cylinder was used to control the relative phase of interaction between the vortices shed by the cylinder and a downstream airfoil engaged in unsteady pitching motion. The interactions resulted in an interruption of airfoil leading-edge vortex shedding process as well as an alteration of the lift history, both of which were found to be dependent on the phase of the disturbances relative to the airfoil kinematics.

Altering the wake pattern of cylinders using splitter plates has been explored by various researchers in the context of vortex-induced vibrations, flow-induced noise, and drag reduction. Cimbala and Garg [21] experimentally studied a circular cylinder with freely rotating splitter plates of various lengths. It was found that the off-axis equilibrium angle that the plate naturally traversed to was impacted by plate length, with smaller lengths resulting in larger angles from the streamwise flow direction. Hasan and Budair [22] investigated the shedding characteristics of a square cylinder having a splitter plate with a range of gap distances. They discovered that gaps smaller than three times the cylinder diameter caused a reduction in shedding frequency compared to the plain cylinder. Gaps beyond this distance led to shedding frequencies comparable to that of the cylinder without a splitter plate. You et al. [23] numerically studied the noise generated by the laminar shedding of circular cylinders at low Reynolds numbers, and found that attaching a splitter plate caused the acoustic quadropole to decrease. Mansingh and Oosthuizen [24] performed wind tunnel tests on a rectangular cylinder with different splitter plate lengths for Reynolds numbers between 350 and 1150. Their study incorporated different plate lengths at several gap distances, and it was discovered that eliminating the gap entirely leads to a drag reduction of approximately 50%.

The use of rotationally oscillating circular cylinders with attached rigid splitter plates for controlled wake generation was demonstrated experimentally by Rockwood and Medina [7]. In comparison with oscillating cylinders, it was found that the cylinders with the splitter plates were able to achieve more consistent cycle-to-cycle shedding, evaluated using the vortex center locations. It was determined that the vortex lock-on, defined as the ability for vortices to be shed at the same frequency as the oscillation frequency, was achieved by the cylinder with attached splitter plate when oscillated at frequencies from 0.3 to 1.1 times the natural shedding frequency. Recent efforts by Chatterjee et al. [25] advanced the experimental efforts of Rockwood and Medina by conducting a numerical investigation on the same cylinder splitter-plate geometry. These studies demonstrated that lift-based vortex lock-on occurred for forcing frequencies 0.8 to 1.4 times the natural shedding frequency when oscillations were kept to smaller amplitudes. Further, Hughes et al. [26] conducted wind tunnel experiments on a similar cylinder splitter-plate geometry at different Reynolds numbers and oscillation amplitudes than that of Rockwood and Medina. Using this cylinder splitter-plate geometry as a disturbance generator, they were able to modulate and annihilate limit-cycle oscillation behaviors in aeroelastic wings.

This paper furthers the exploration of rotating circular-cylinder-splitter-plate disturbance generators by investigating and comparing the wake and load characteristics for various geometries. The details of the computational setup used in the current study are provided in Sec. II. Through a parametric study of rotating cylinders with various plate lengths, we aim to correlate the trends in the flowfield and loads to the splitter plate lengths and to compare the observations with both stationary and rotating cylinders without plates. The findings of the study are described in Sec. III. We look to identify near-wake characteristics determining the vortex formation and wake generation patterns, and far-field features such as coherency of the vortex structures and local flow angle variations. Correlation between fundamental frequencies of both force coefficients and downstream velocities are also reported. The findings not only help to determine the effectiveness of the disturbance generators, but also to create a map that will aid in low-order modeling of the flowfield features and disturbance generator design. Finally, the conclusions are outlined in Sec. IV.

II. Computational Setup

Circular cylinders with and without splitter plates undergoing sinusoidal oscillations were studied using a two-dimensional unsteady Reynolds-averaged Navier–Stokes (RANS) approach. The commercial computational fluid dynamics (CFD) software package ANSYS Fluent 20.1 was used to carry out the numerical simulations. Although the flow around bluff bodies is inherently three-dimensional outside of very low Reynolds numbers, appreciable results from two-dimensional simplifications for circular cylinder cases have been demonstrated previously by Stringer et al. [27]. The geometries studied here were identical to those used in water tunnel experiments performed by Rockwood and Medina [7]. Cases with the attached splitter plate had plate lengths ℓ varying from $0.25d$ to $1.25d$, where d is the cylinder diameter. A list of cases studied in this research is provided in Table 1. The plate thickness was set to $0.126d$ for each case that had a splitter plate.

A structured O-type mesh was utilized for every geometry tested. The large oscillation amplitudes prescribed to the geometries required a dynamic meshing approach that allowed the cell structure to be maintained throughout the cycle, absent of excessive skewness in the region near the cylinder. This was accomplished by splitting the domain into two zones: an inner region surrounding the geometry and an outer region that remained stationary. Dynamic motion was applied to the inner region that contains the disturbance generator, and field variable information was passed through an interface to the stationary outer region at each time step. Figure 1 shows an overview of the computational domain including the interface between both regions, as well as the near-wall mesh details for the case of $\ell/d = 1$.

Table 1 List of cases

Case	Rotation	Splitter plate length, ℓ/d	Element count
1	No	0	77,560
2	Yes	0	77,560
3	Yes	0.25	114,950
4	Yes	0.5	119,790
5	Yes	0.75	124,630
6	Yes	1	129,470
7	Yes	1.25	134,310

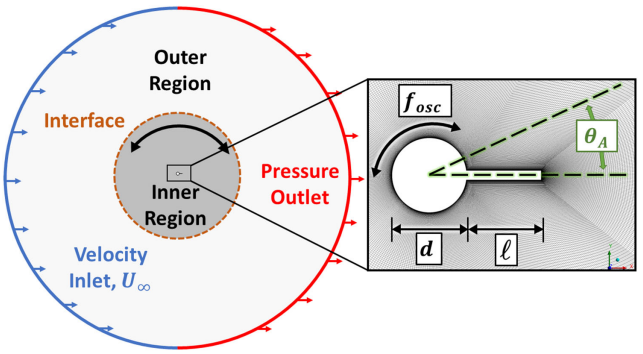

Fig. 1 Overview of the computational domain showing the region partitions and boundary conditions, as well as near-wall mesh details and parameter definitions (inset).

This approach of partitioning the domain into oscillating and stationary regions also reduces the computational expense associated with deforming mesh strategies. The extents of both the inner and the outer regions were identical for all geometries tested. Sufficiently large domain extents were employed in place of replicating the dimensions of the test section from water tunnel experiments. The diameter of the circular interface between the regions is $40d$, while the outer region representing the velocity inlet and pressure outlet had a diameter of $110d$.

A grid refinement study was performed on the baseline cylinder with attached splitter plate case ($\ell/d = 1$) in order to obtain the discretization error introduced by successively finer grids. The Grid Convergence Index (GCI) method described by Celik et al. [28] was used to find the discretization uncertainty of the time-varying lift coefficient on three grid levels. Grid refinement was conducted by changing the growth rate in the boundary-layer region while maintaining identical first layer cell heights. Additionally, surface cell counts were systematically increased for finer grids in order to maintain cell aspect ratios. The three grid levels are shown in Fig. 2.

For the three levels of refinement tested, root mean square (RMS) values of C_L were shown to decrease monotonically with average cell size, as listed in Table 2. The discretization uncertainty of $C_{L,\mathrm{RMS}}$ on the fine grid was found to be 0.69%, and so this grid level was chosen to be the basis for the other grids with varying splitter plate lengths.

Using the fine grid, the cases without splitter plates ($\ell/d = 0$) had a total of 280 cells along the cylinder surface, while the cylinder with the largest splitter plate tested ($\ell/d = 1.25$ case) had 555 cells. The near-wall region was fully resolved, with a first layer cell height of $1.2 \times 10^{-3} d$ ensuring a y^+ value below 1 across the entire surface. A total of 32 cells covered the boundary-layer region with a growth rate of 1.05. The velocity inlet was prescribed a uniform streamwise velocity and a turbulence intensity of 0.1%. Due to the large domain extents, solutions were checked to ensure that turbulence intensity values did not decay before reaching the disturbance generator. Using water as the working fluid and cylinder diameter d as the characteristic length results in a Reynolds number of 7600, identical to the experiments performed by Rockwood and Medina [7]. The $k-\omega$ shear stress transport (SST) turbulence model was chosen over other eddy-viscosity models due to favorable results when simulating unsteady circular cylinder flows at moderately low Reynolds numbers [29]. The SST model has also been found to better handle moderate shear conditions [30], which is important in capturing the shear layer interaction that occurs near the splitter plate edge in the present work. The Semi-Implicit Method for Pressure Linked Equations (SIMPLE) was utilized for pressure-velocity coupling, and pressure and momentum spatial discretization was second-order accurate. A nondimensional time step of $t^* = 2.95 \times 10^{-3}$ was used for all the oscillating cases, while the stationary cylinder case was run using $t^* = 2.95 \times 10^{-2}$. Residuals were driven to below 7×10^{-5} at each time step. Appending the $k-\omega$ SST turbulence model with a one-equation transition model was considered, but testing on the baseline cylinder with attached splitter plate case did not show appreciable differences in surface forces or vortex formation. Hence the one-equation transition model was not included considering the additional computational cost.

Table 2 Grid refinement levels for the baseline case

Refinement level	Cell count	Average cell size	$C_{L,\mathrm{RMS}}$
Coarse	32,428	0.0861	8.42
Medium	73,528	0.0572	8.36
Fine	129,470	0.0431	8.35

While the advantages of the $k-\omega$ SST turbulence model are apparent with regard to other eddy-viscosity RANS models, a discussion on the accuracy of cylinder forces is warranted for subcritical Reynolds numbers such as the one considered in this work. It is known that unsteady RANS (URANS) simulations at these Reynolds numbers suffer from difficulty in predicting the laminar to turbulent transition in the detached shear layers for stationary and rotating plain cylinders when compared to experiments and higher-fidelity simulations such as large-eddy simulations (LES) and direct numerical simulations (DNS). As such, eddy-resolving methods are better suited to discern the spectral content of time-varying cylinder forces for these flows. The inclusion of a splitter plate in this study, however, pushes the issue of shear layer transition beyond the scope of naturally shedding cylinders. Therefore, we have elected to proceed with unsteady RANS simulations for the present work. We present comparisons to prior work also utilizing the $k-\omega$ SST turbulence model to demonstrate that the predicted time-averaged drag coefficients are close to the values published for low-Reynolds-number flows. Table 3 shows comparisons of the results from the current mesh and solver methodology with the URANS results of Rosetti et al. [31] for both laminar and subcritical Reynolds numbers for a stationary circular cylinder.

It is seen that the drag coefficients generally agree with the results of Rosetti et al., but both methods overpredict drag when compared to prior experiments [32], as is expected.

As the work presented here is primarily focused on rotationally oscillating bluff bodies, we have also produced comparisons of time-averaged lift and drag forces with DNS solutions of rotating cylinders published by Aljure et al. [33] for two rotation ratios at $Re = 5000$, shown in Table 4. The rotation ratio is defined as the ratio of tangential cylinder velocity U_T to freestream velocity U_∞.

Table 3 Average C_D comparison with the results of Rosetti et al.

Reynolds number	Rosetti et al.	Our current work
200 (Laminar)	1.31	1.27
1,000	1.44	1.24
10,000	1.52	1.60

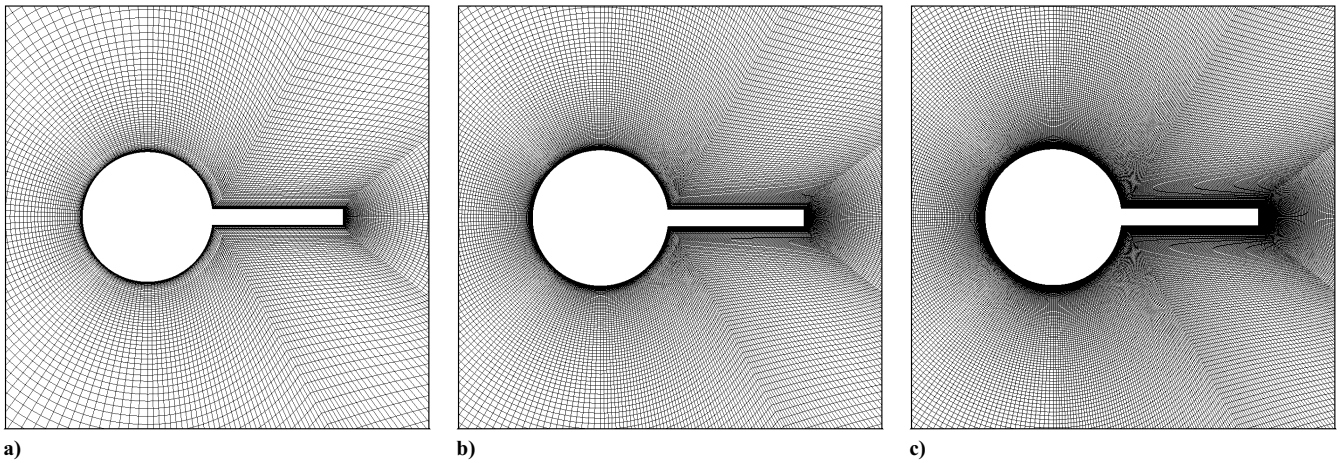

a) b) c)

Fig. 2 Mesh density in the region near the disturbance generator: a) coarse, b) medium, c) fine.

Table 4 Comparison of average C_L and C_D with the results of Aljure et al.

	Aljure et al.		Our current work	
U_T/U_∞	C_L	C_D	C_L	C_D
1	1.4	0.9	1.92	1.13
2	4.47	0.36	4.92	0.17

General agreement is found for both lift and drag, as well as the trends of increasing lift and decreasing drag for higher rotation rates due to shrinking of the shear layers and biasing of the wake. A sizeable error of 52% for the drag coefficient is seen for the larger rotation rate. The mechanisms responsible for this low drag number, however, are not present during oscillatory rotation with the addition of splitter plate, as will be discussed in Sec. III.

Qualitative validation of the wake produced by sinusoidally oscillating cylinders with attached splitter plates ($\ell/d = 1$) was performed through comparisons with the experimental results of Rockwood and Medina [7]. The rotational motion is given by

$$\theta(t) = \theta_A \sin(2\pi f t) \tag{1}$$

where θ is the rotation angle measured clockwise (CW) with respect to the streamwise flow direction, θ_A is the maximum oscillation amplitude, f is the frequency, and t is time. The flowfield predictions were compared against particle image velocimetry (PIV)-generated vorticity contours from the work of Rockwood and Medina [7] for cases with different oscillation frequencies and maximum amplitudes. A total of four cases were selected based on the differing wake structures, including cases having complex wakes with irregular vortex streets. The validation results are shown in Fig. 3. The frequencies selected were various fractions of the natural shedding frequency of a stationary circular cylinder, f_n. It must be mentioned that the natural Strouhal number for the stationary cylinder from the current work was found to be $St = 0.224$, corresponding to a natural shedding frequency of 2.65 Hz. This value is larger than the Strouhal number of $St = 0.202$ from the experiments of Rockwood and Medina [7]. Such experiment-CFD deviation in the natural Strouhal number has also been observed by Rosetti et al. [31] and is not abnormal for subcritical cylinder flows solved using the $k-\omega$ SST turbulence model.

Vorticity contours obtained from the current CFD methodology show good agreement with experimental results for all the cases. For the cases where $f = 0.3f_n$, the irregular wake pattern is accurately replicated in the numerical simulations. There is a small discrepancy in the position of the negative shear layer near the cylinder body for comparison case (a), but the shear layer roll-up behind the cylinder is adequately captured near the splitter plate, as is the location of both CW and counterclockwise (CCW) vorticity. For the cases of coherent vortex wake generation ($f = 0.7f_n$ and $f = 1.0f_n$), the CFD-predicted wake structures are comparable to those from the water tunnel experiments. Comparison cases (b) and (c) show the presence of additional negative vorticity in the top right quadrant of the surveyed area in the simulations. This vorticity is the attributed to the overall vortex street, which cannot be seen due to the contour levels around near-zero vorticity being excluded. It is evident that the RANS simulations slightly underpredict the dissipation rate of the vortex cores as they convect downstream. Additionally, there is minor disagreement in the streamwise location of the vortex strand initially shed for the case of $f = 0.7f_n$, but the downstream vortex spacing is still accurate in this case. Overall, the results from the present two-dimensional CFD approach are consistent with the experimental observations, and are therefore used to conduct a detailed study of several geometries.

III. Results

We now conduct a detailed study on the various geometries listed in Table 1 to characterize the wake generated by them and to analyze the associated loads. All the cases presented here have the same cylinder diameter and freestream velocity. For the rotating cases, the geometries are sinusoidally oscillated about the axis of the cylinder at the baseline stationary circular-cylinder natural shedding frequency f_n. Preliminary simulations on the stationary cylinder case yielded a natural shedding frequency of $f_n = 2.65$ Hz, and this value was used as the oscillation frequency for all cases presented here. The maximum oscillation amplitude θ_A is set to $\pi/4$ for all cases. The cycle start time $t/T = 0$ corresponds to the position of the splitter plate being parallel to the freestream flow. From here, the oscillation cycle begins with rotation occurring in the CCW direction. For the stationary cylinder case, cycle start time is taken to correlate with the natural shedding frequency. That is, each cycle period starts and ends at some multiple of $1/f_n$ from the simulation start time $t = 0$. The initial transient period for the stationary cylinder case lasted 40 shedding cycles before data collection. Oscillating cases required 10 cycles before data could be taken, with the

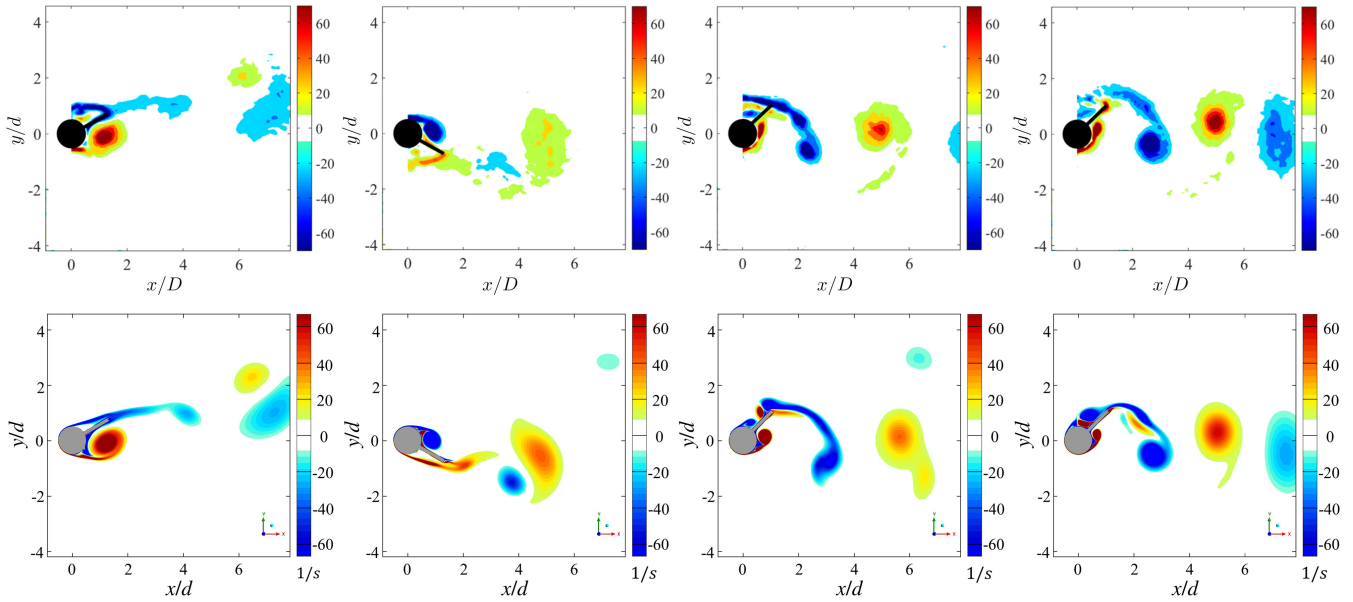

Fig. 3 Experimental validation of wake vorticity. Top row: Water tunnel experiment PIV. Bottom row: CFD using present methodology. PIV images reproduced from [7] with permission.

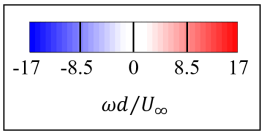

Fig. 4 Nondimensional vorticity colorbar for the contour plots presented in this paper.

longest splitter plate cases requiring far less time to exhibit fully periodic force and wake results. For the vorticity contour plots discussed in this section, the colorbar shown in Fig. 4 should be used.

A. Flowfield

The mechanisms involved in the generation of vortex-dominated wakes shed by stationary circular cylinders are well-established in the literature [8,34], and therefore will not be discussed in detail here. In the case of a stationary cylinder, shed vortices are formed by the interaction of shear layers with opposite-signed vorticity forming on upper and lower surfaces of the cylinder. For example, a CW vortex is shed into the wake when the shear layer with CCW vorticity from the lower surface impinges on the shear layer with vorticity rolling up on the upper surface, thereby causing the rolled up CCW shear layer to detach and convect downstream. In the case of a rotationally oscillating cylinder, the rotations affect these shear-layer interactions intermittently because the shear layers on either side of the stagnation point are accelerated or decelerated due to the rotation of the cylinder.

Figure 5 shows the evolution of vorticity in the near region of the rotating cylinder case, $\ell/d = 0$. The vortex shedding process for this case is symmetric about the half-cycle time, and so only the first half of the cycle is presented. That is to say, the vorticity flowfield for $t/T = 8/16$ is a mirror image about the streamwise centerline of the flowfield for $t/T = 0$, although with opposite sign. Between $t/T = 0$ and $t/T = 4/16$, a secondary CCW shear (red color in Fig. 5) layer can be seen forming along the trailing edge of the cylinder on the upper surface and progressing CW (matching the cylinder motion for this portion of the cycle). From $t/T = 5/16$ to $t/T = 7/16$, it begins to lift off from the cylinder surface due to the influence of the rolled up CW structure located downstream. The lifted-off CCW shear layer then interrupts the CW layer feeding the rolled-up structure, and causes the CW shear layer to detach completely and form a vortex by $t/T = 8/16$ (not shown, but visualized as a streamwise reflection of $t/T = 0$). The CW vortex formation is thus more abrupt compared to a classic stationary cylinder case where the detachment would not take place until the primary shear layer from the lower surface interrupts the rolling CW shear layer on the upper surface. The secondary CCW shear layer dissipates quickly in the subsequent time steps after the CW vortex is shed into the wake. This process repeats on the lower surface during the second half of the cycle.

The addition of a splitter plate has two effects on the vortex formation process. The first is the blocking of the shear layers on either side of the cylinder from interacting, which moves their mixing point further downstream from the cylinder. The second effect is the formation of an additional "edge" vortex along the trailing edge of the splitter plate that interacts with the shear layers and modifies the vortex shedding pattern. The length of the splitter plate affects both the shift in the shear-layer mixing location as well as the strength of the trailing-edge edge vortex, and thus ultimately the spatiotemporal characteristics of the wake.

Figure 6 shows the evolution of vorticity in the near wake of the $\ell/d = 0.25$ case. At $t/T = 0$, a CW edge vortex can already be seen forming at the trailing edge of the splitter plate. The snapshot at $t/T = 3/16$ shows that this edge vortex is continuously fed by the CW shear layer formed on the upper surface. Also note the location and size of the lower-surface CCW shear layer roll-up between $t/T = 0$ and $t/T = 4/16$ compared to the $\ell/d = 0$ case. During this time period, the primary CCW shear layer remains below the splitter plate due to the blockage effect of the plate, and it does not lift away from the cylinder surface in the same way as the $\ell/d = 0$ case. Instead, the shear layer elongates in the direction of the splitter plate due to the influence of the CW edge vortex. This shear layer interacts with the growing edge vortex, causing it to eventually detach and convect into the wake. In contrast to the $\ell/d = 0$ case, the secondary CCW vorticity on the top surface does not play a role in the detachment process. The CW vortex is shed much earlier in the cycle, with pinchoff identified at $t/T = 6/16$. From here, the cycle begins to repeat itself, and the formation of a CCW edge vortex occurs at $t/T = 8/16$ (not shown, but visualized as a streamwise reflection of $t/T = 0$).

Figure 7 shows the evolution of vorticity in the near region of the $\ell/d = 0.5$ case. This is the only case in which a fully asymmetric wake is generated by the cylinder with attached splitter plate. Looking at $t/T = 0$, a CW edge vortex can already be seen forming below the splitter plate just as in the $\ell/d = 0.25$ case. This edge vortex is fed by a larger amount of shear layer vorticity than the previous case. Also apparent is the additional roll-up of the CW vorticity on the upper surface of the splitter plate. This roll-up occurred in the $\ell/d = 0.25$ case, but to a lesser degree. The CCW sweeping motion of the splitter plate halts this roll-up and forces the CW shear layer to continue feeding the edge vortex. This constructive interaction of the cylinder and edge vortices has recently been observed by Sunil et al. [35] for the case of a cylinder having a flexible splitter plate of $\ell/d = 2$ oscillating to 5° at $f = 1.7f_n$. The constructive interaction resulted in increased vortex strength, thereby causing a greater velocity deficit in the wake. A similar trend in the current work is discussed later in this section. Unlike the $\ell/d = 0$ and $\ell/d = 0.25$ cases, the CW vortex shed in the $\ell/d = 0.5$ case is influenced significantly neither by the secondary CCW vorticity on the upper surface nor by the CCW shear layer from the lower surface. This delays the detachment of the CW vortex back to $t/T = 7/16$, by which point a CCW edge vortex has already formed

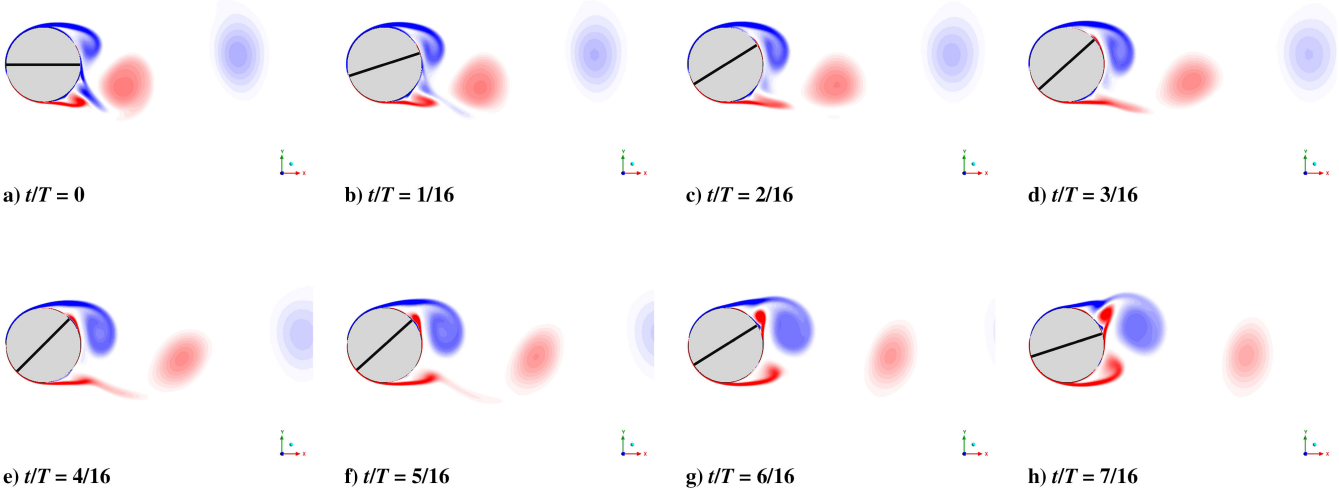

Fig. 5 Case 2: vorticity contours over half a cycle for the case of $\ell/d = 0$.

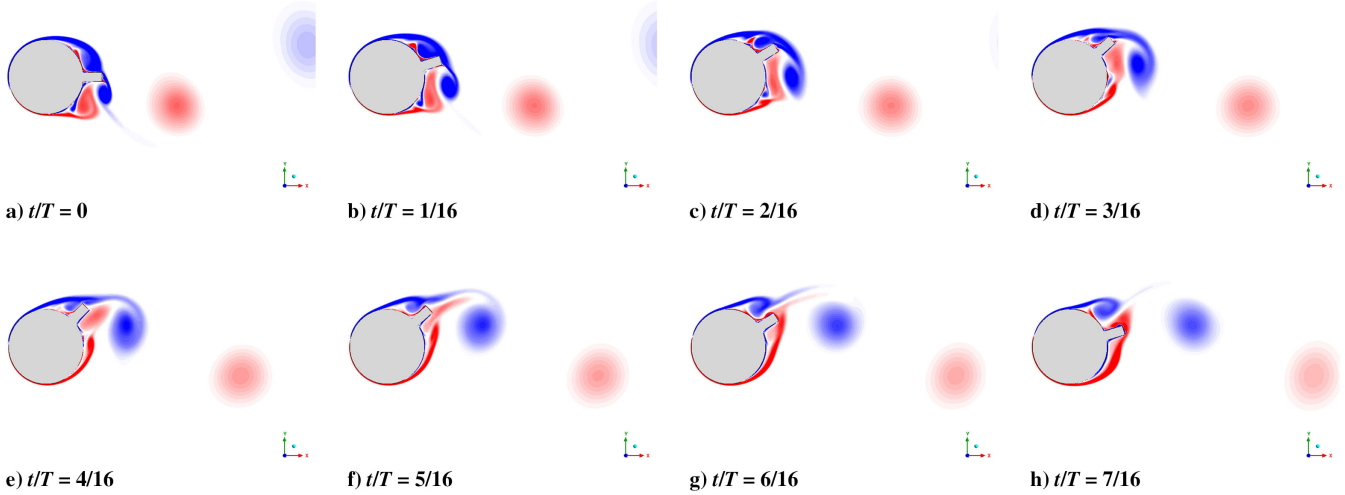

Fig. 6 Case 3: vorticity contours over half a cycle for the case of $\ell/d = 0.25$.

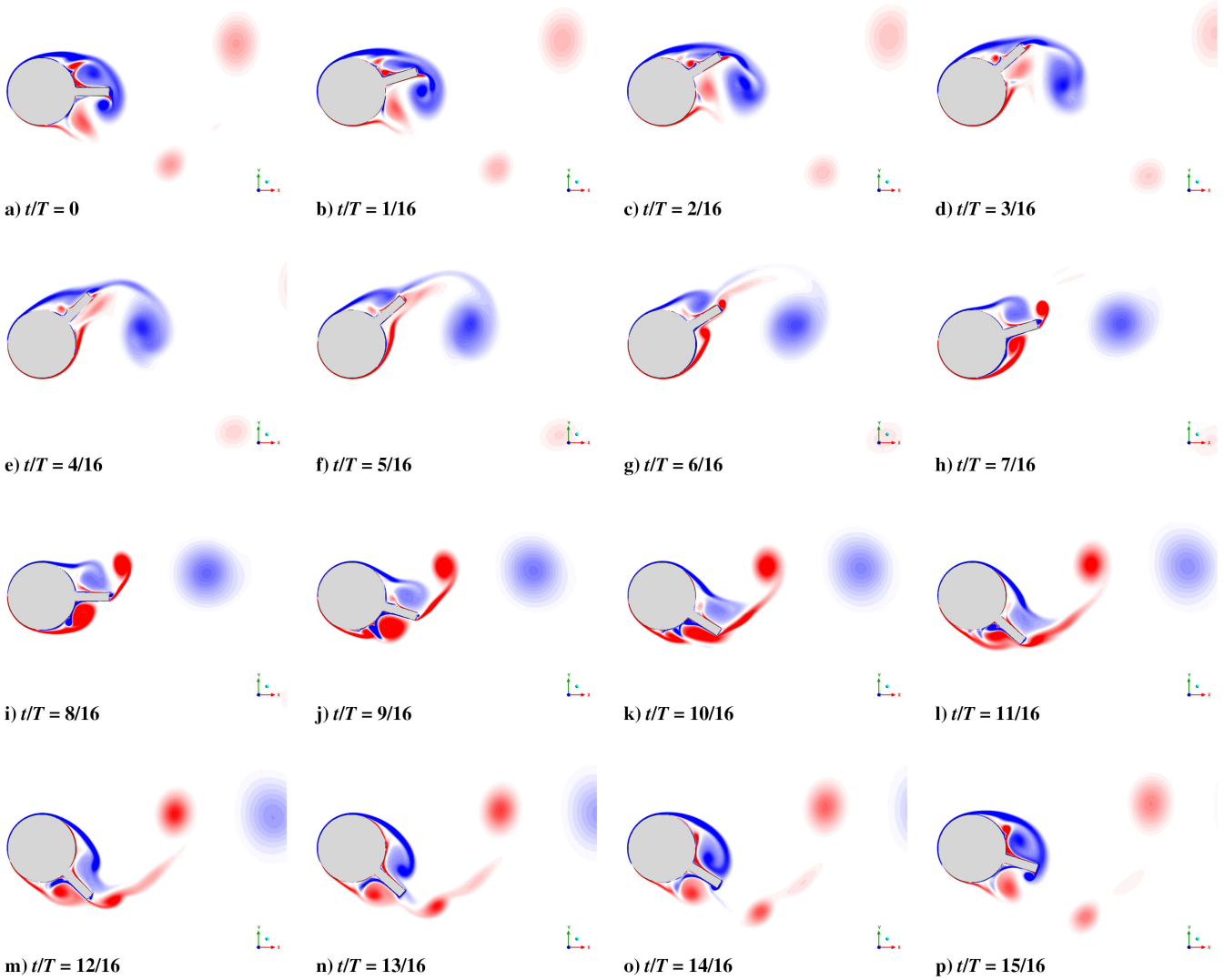

Fig. 7 Case 4: vorticity contours over a full cycle for the case of $\ell/d = 0.5$.

on the plate trailing edge. At the same time, CCW shear layer roll-up occurs much closer to the region where the plate connects to the cylinder. As a result, the CCW edge vortex is not fed by the shear layer roll-up unlike in the first half of the motion, and so a much weaker CCW edge vortex is formed and shed earlier in the cycle. This is most obvious when comparing the images at $t/T = 0$ and $t/T = 8/16$, when the plate is aligned with the flow centerline. This asymmetry in vortex formation is apparent in the wake, which has vortex triplets rather than alternating-sign vortices. A similar transition to wake asymmetry in flapping foils has been previously observed by Godoy-Diana et al. [36] and Das et al. [37]. Their work associated the deflection of pitching foil wakes with higher forcing frequencies. This is comparable to the present work, where increasing plate length results in larger edge velocities.

The $\ell/d = 0.75$ case exhibits a return to wake symmetry as can be noticed from the flow images in Fig. 8. It also marks the first case in which a reverse wake occurs, with CW vortices in the wake located below the wake centerline, and CCW-signed vortices located above it. At the beginning of the cycle, the combination of a CW edge vortex and CW shear layer roll-up can be seen to occur similar to what has been described in the previous splitter-plate cases. Unlike the $\ell/d = 0.25$ and $\ell/d = 0.5$ cases, however, the CW-signed edge vortex is not significantly fed by the shear layer roll-up above the splitter plate. This is similar to the latter half of the $\ell/d = 0.5$ case, where the edge vortex is the prominent flow feature due to blockage created by the plate. Going from $t/T = 0$ to $t/T = 6/16$ (when complete CW vortex formation occurs), the rolled-up shear layer above the splitter plate largely remains located in the same position during the CCW sweep of the disturbance generator. The increased velocity of the splitter plate edge (due to larger splitter plate length) also means that the edge vortex initiation occurs much earlier in the cycle. The formation of the CW vortex begins during the previous cycle at $t/T = 13/16$ (not shown, but visualized as a streamwise reflection of $t/T = 5/16$), just after the cylinder starts rotating CCW. This early edge vortex formation coupled with a CCW roll-up that occurs beneath the splitter plate results in the CW vortex being shed when the plate edge is below the wake centerline.

The reverse wake phenomenon also occurs for the cases with $\ell/d = 1$ and $\ell/d = 1.25$, for which half-cycle vorticity contours are shown in Figs. 9 and 10, respectively. Similar to the $\ell/d = 0.75$ case, the edge vortex remains the most prominent contribution to wake formation. The blockage effect due to the splitter plate still largely prevents the shear layer from interacting with the edge vortex. Much like the $\ell/d = 0.75$ case, shear-layer vorticity of opposite sign to the edge vortex contributes to the detachment of the edge vortex at $t/T = 5/16$. The formation and propagation of vorticity in the near region of the geometry is largely identical between these final two cases. The main difference between the final three cases is the strength of the edge vortex and its location relative to the cylinder center. The increased edge velocity due to larger plate lengths causes the edge vortex strength to become larger, as expected. Upon visual inspection, increasing plate length results in the edge vortex core being located further from the cylinder. Its distance and position relative to the edge of the plate, however, largely remains constant.

A quantitative comparison of the circulation values in the wake between various configurations is shown in Fig. 11. The circulation Γ is obtained using

$$\Gamma = \iint_A \omega \cdot \mathrm{d}A \tag{2}$$

where A is the integration area and ω is vorticity. The vorticity information was gathered in a rectangular region spanning from $x/d = 4$ to $x/d = 6$ and from $y/d = -2.5$ to $y/d = 2.5$, sketched in Fig. 11a. This area is identical to that used in the study by

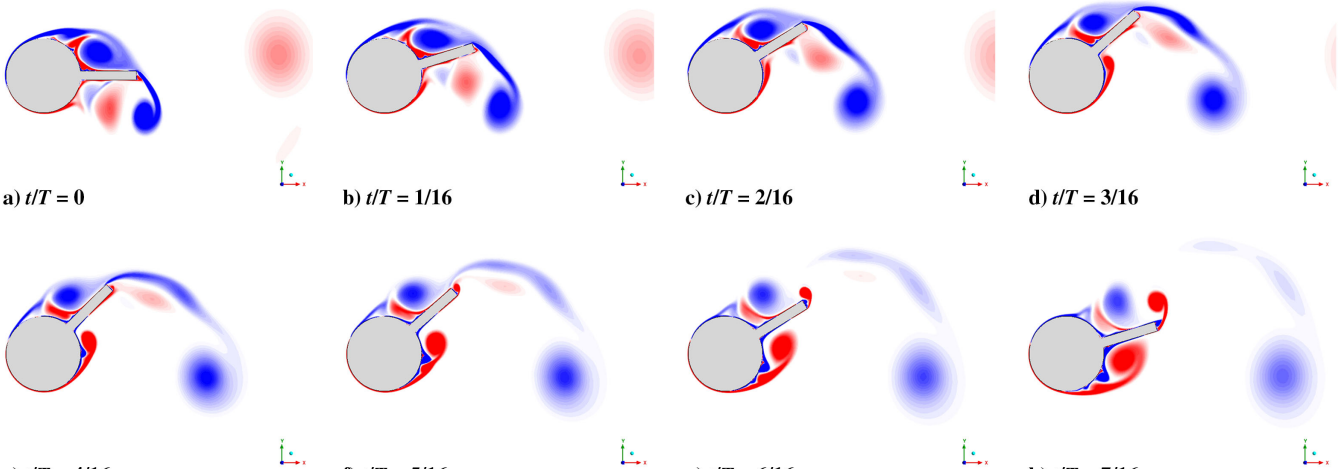

a) $t/T = 0$ b) $t/T = 1/16$ c) $t/T = 2/16$ d) $t/T = 3/16$

e) $t/T = 4/16$ f) $t/T = 5/16$ g) $t/T = 6/16$ h) $t/T = 7/16$

Fig. 8 Case 5: vorticity contours over half a cycle for the case of $\ell/d = 0.75$.

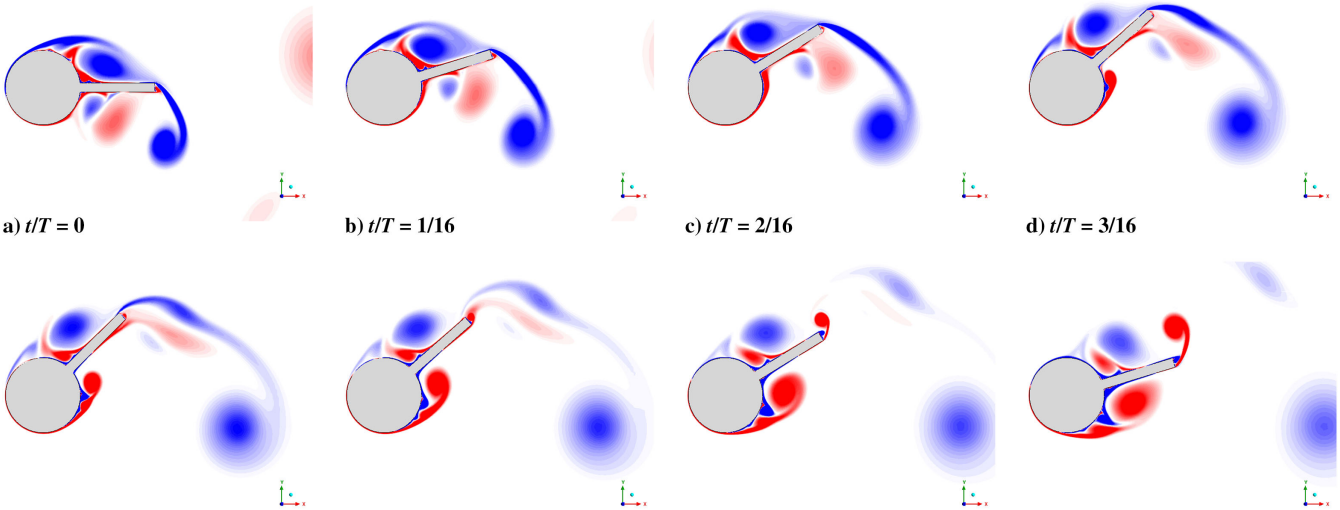

a) $t/T = 0$ b) $t/T = 1/16$ c) $t/T = 2/16$ d) $t/T = 3/16$

e) $t/T = 4/16$ f) $t/T = 5/16$ g) $t/T = 6/16$ h) $t/T = 7/16$

Fig. 9 Case 6: vorticity contours over half a cycle for the case of $\ell/d = 1$.

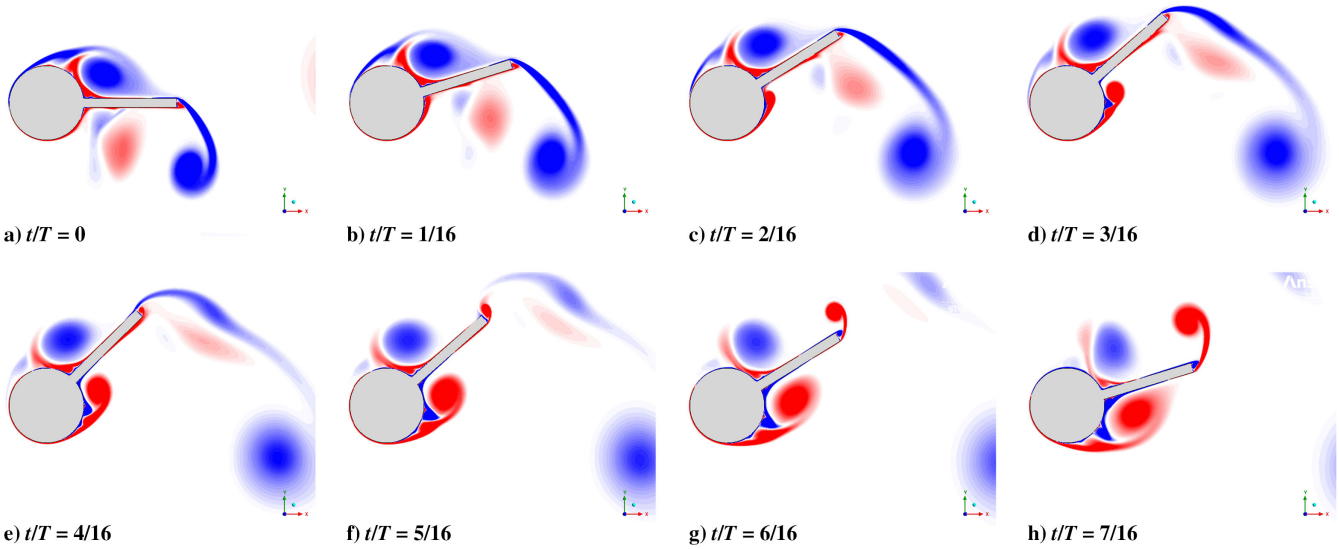

Fig. 10 Case 7: vorticity contours over half a cycle for the case of $\ell/d = 1.25$.

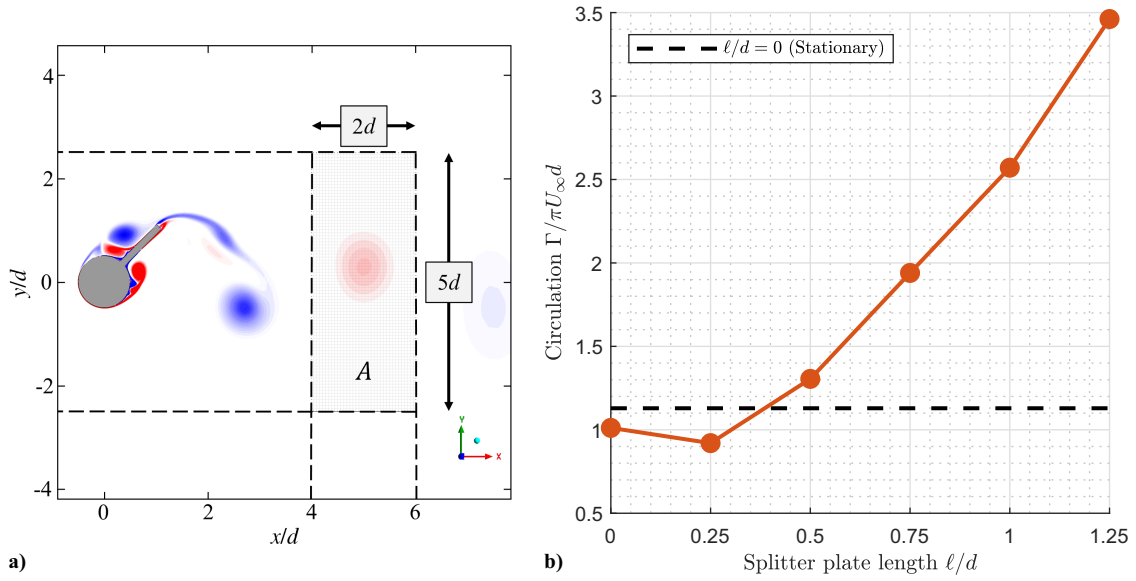

Fig. 11 Circulation progression for increased splitter plate length. a) Integration region used to compute circulation. b) Plot of normalized circulation for various splitter plate lengths.

Rockwood and Medina [7], although the calculation of circulation presented in the current work includes both negative and positive vorticity values. The time instant used for the circulation calculation was taken to be when a primary CCW vortex was approximately centered within the integration window. The strength of the vortices produced by the stationary cylinder is indicated by a dashed line. The oscillating plain cylinder results in weaker vortices than the stationary cylinder. This contrasts with the findings of Rockwood and Medina [7]. Adding a splitter plate of $\ell/d = 0.25$ further decreases the vortex strengths, indicating that a destructive interaction occurs during vortex formation. This negative interference is evident when looking at the shear layer interaction compared between case 2 and case 3 (Figs. 5 and 6, respectively). While the CCW shear layer is responsible for the detachment of a CW vortex early in the cycle for both cases, the influence of this CCW shear layer varies between the cases. For the case of $\ell/d = 0.25$, the CCW shear layer beneath the splitter plate encompasses a large area, and its proximity introduces a reduction in strength of the CW edge vortex before shedding. Increasing the splitter plate length to $\ell/d = 0.5$ indicates the first case tested in which the vortex strength is larger than the stationary cylinder case. Further increase in plate length results in much stronger vortices shed into the wake.

B. Loads on the Cylinder

The investigation of fluid-dynamic loads experienced by the bodies is not only important from the perspective of structural or propulsive considerations, but is also useful for identifying the occurrence of vortex shedding events in the absence of flow diagnostics capabilities. This section discusses the effect of splitter-plate length on the single-cycle coefficients of lift, drag, and pitching moment. The lift coefficient C_L, the drag coefficient C_D, and the pitching moment coefficient C_M are defined as

$$C_L = \frac{F_L}{(1/2)\rho U_\infty^2 d} \tag{3}$$

$$C_D = \frac{F_D}{(1/2)\rho U_\infty^2 d} \tag{4}$$

$$C_M = \frac{M}{(1/2)\rho U_\infty^2 d^2} \tag{5}$$

where F_L represents lift, F_D represents drag, and M represents the pitching moment about the cylinder center, per unit span. The reference density and the reference velocity are indicated by ρ and U_∞, respectively. Single-cycle lift histories for all the geometries are presented in Fig. 12. The lift history for the stationary cylinder in Fig. 12a is sinusoidal as expected, with C_L reaching ± 1.72. Choosing the cycle start and end time to be a multiple $1/f_n$ results in the zero crossing of lift occurring at $t/T = 0.43$. For the oscillating circular cylinder ($\ell/d = 0$), the maximum and minimum lift values are lower in magnitude compared to that of the stationary cylinder as a result of the weaker vortices shed into the wake. The zero crossing of lift occurs at a cycle time of $t/T = 0.38$.

A significant deviation from the sinusoidal lift pattern occurs for the first time for $\ell/d = 0.25$. An excessive drop in lift occurs during the first half of the cycle. A lift gain occurs during the second half of the cycle, although it is not a mirror image of the magnitude difference seen during the first half of the cycle. Moving on to the cases presented in Fig. 12b, it becomes obvious that the trend beyond $\ell/d = 0.25$ is toward lift magnitudes that peak at the beginning, middle, and end of the oscillation cycle. The magnitudes are significantly higher than that of the previous three cases in Fig. 12a. The difference in magnitude between the maximum and the minimum lift increases for increasing plate lengths. The case of $\ell/d = 0.5$ is still asymmetric about the half-cycle time, but a triangle waveform begins to develop for longer plate lengths. The shift from sinusoidal to triangle waveforms naturally results from the increased prominence of the edge vortex that forms along trailing edge of the splitter plate. Additionally, these lift-magnitude peaks correspond to cycle times at which the splitter plate velocity is at a maximum, thus leading to force peaks occurring on the splitter plate at these time instants.

The drag histories are presented in Fig. 13. The drag curves display trends similar to the lift curves in terms left-right symmetry, irregularity, and peak magnitudes, although at twice the frequency. The large-plate-length cases in Fig. 13b exhibit short intervals of negative drag. Despite the short intervals of negative drag and the reverse wake pattern occurring in these larger-plate-length cases, the mean drag remains positive for all the cases studied here and in fact increases

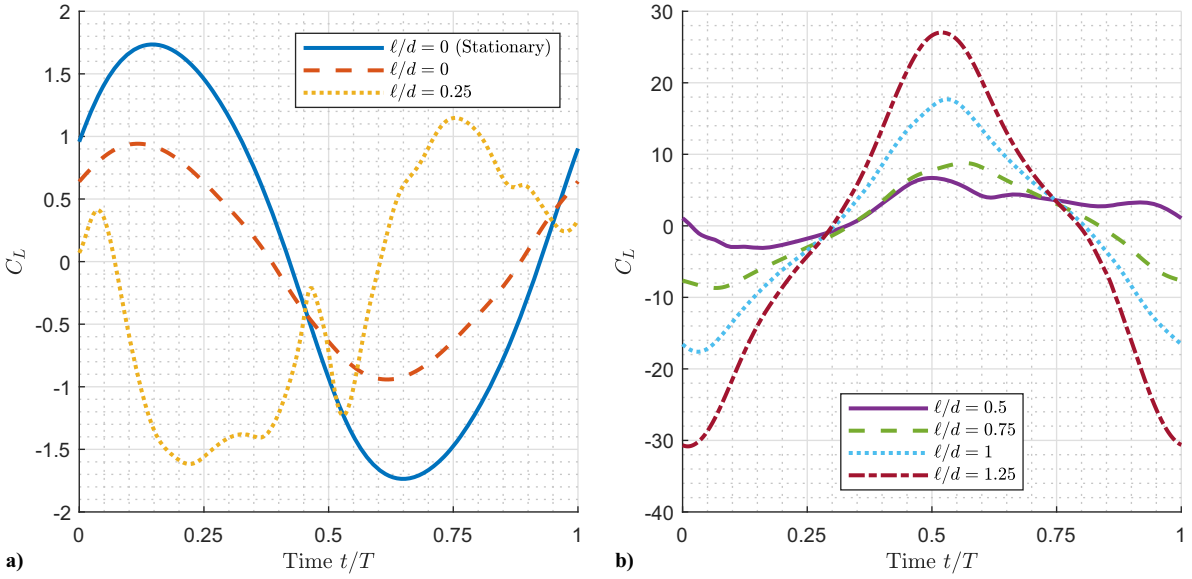

Fig. 12 Lift coefficient plots for a complete cycle: a) $\ell/d = 0$ (stationary), $\ell/d = 0$, and $\ell/d = 0.25$; b) $\ell/d = 0.5$, $\ell/d = 0.75$, $\ell/d = 1$, and $\ell/d = 1.25$.

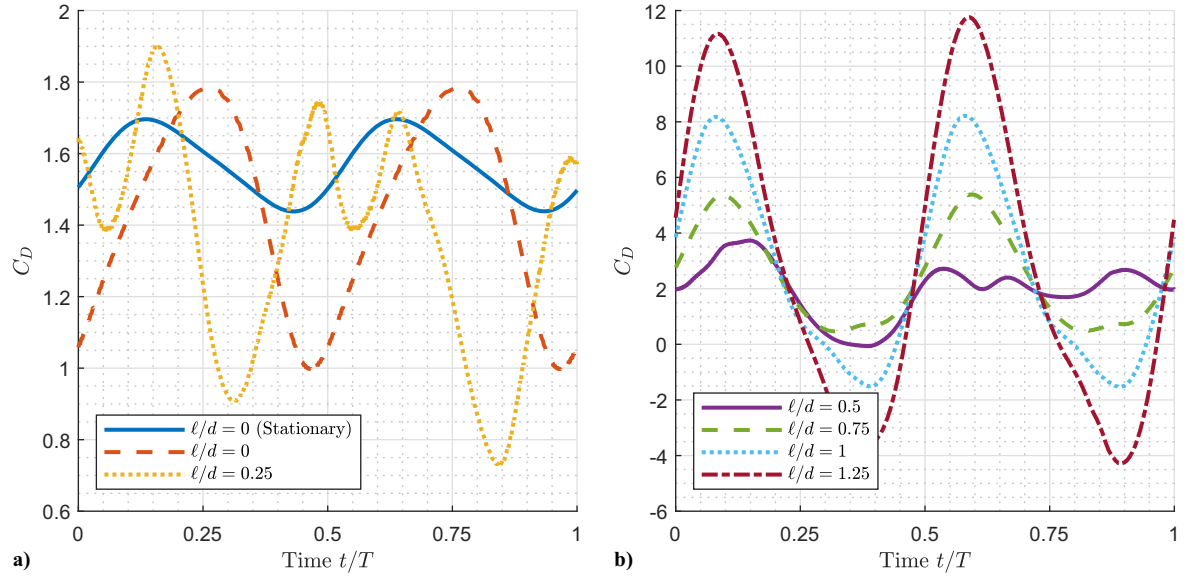

Fig. 13 Drag coefficient plots for a complete cycle: a) $\ell/d = 0$ (stationary), $\ell/d = 0$, and $\ell/d = 0.25$. b) $\ell/d = 0.5$, $\ell/d = 0.75$, $\ell/d = 1$, and $\ell/d = 1.25$.

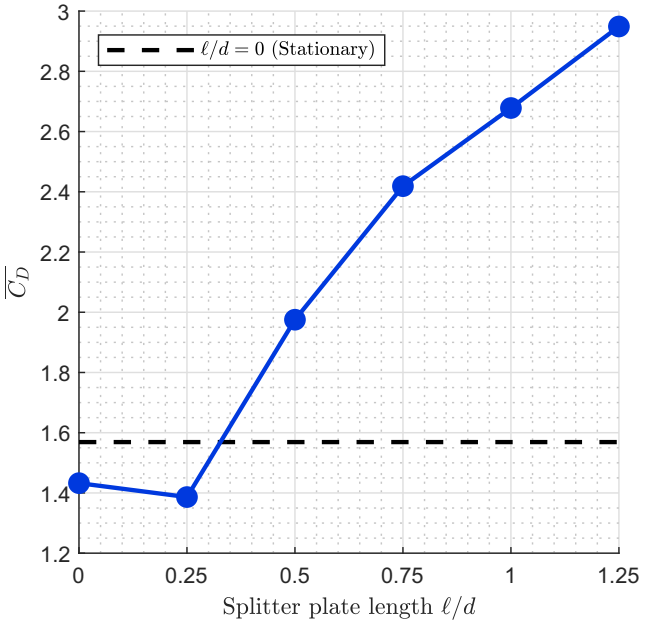

Fig. 14 Time-averaged drag coefficient values for various splitter-plate lengths.

with splitter-plate length in the larger-plate-length regime. Figure 14 shows the change in time-averaged C_D for each geometry in comparison to that of the stationary cylinder. It can be seen that oscillating the plain cylinder at the natural shedding frequency results in a mean drag lower than that of the stationary cylinder. This pattern has been reported before by Cheng et al. [38]. This is also the case for $\ell/d = 0.25$, with the drag being slightly lower than $\ell/d = 0$. The reduced drag in these cases can be attributed to the weaker vortices shed as shown in Figs. 5 and 11b. Further increasing the splitter-plate length beyond $\ell/d = 0.25$ leads to a monotonic increase in average drag, as was also seen with the circulation in Fig. 11b.

Figure 15 shows the pitching moment histories for all the geometries. The pitching moment magnitudes are relatively insignificant for the stationary and rotating circular cylinders without the splitter plates. Interestingly, the overall trends are similar to the lift history for the cases with splitter plates. A nonsinusoidal, nonsymmetric pitching moment variation is seen for the case with $\ell/d = 0.25$. A sudden jump in magnitude is observed for $\ell/d = 0.5$. Similar to the lift variation, the peak magnitude values increase for higher splitter plate lengths with the maximum occurring at midcycle and minima occurring at the start and end of the cycle. Additionally, the two halves of a cycle generally become more symmetric with increasing plate length.

A further look at the frequency content of the loads is beneficial for classifying unsteadiness in the forces. For brevity, the current discussion is limited to lift. A comparison of the lift-coefficient fast Fourier transforms (FFTs) for the stationary cylinder and cylinders with various splitter plate lengths is shown in Fig. 16. A total of 12 oscillation cycles were used to calculate FFT values for all the cases presented. It is clear that the stationary-cylinder force curve is rather clean with the dominant peak at the vortex shedding frequency. It also displays a secondary low-magnitude peak at 7.94 Hz, which is exactly three times the primary frequency of lift. Every oscillating geometry studied here shows a primary frequency that matched the oscillation frequency. This should be expected, as the movement of the disturbance generator is the defining feature of the force curve. The oscillating cylinder case ($\ell/d = 0$) is very close in form to the stationary cylinder, with the largest difference being the amplitude of the dominant frequency. Irregularities first begin to appear in the $\ell/d = 0.25$ case. The C_L FFT for this case is distinguished by several spikes at various frequencies. Within the range of the frequencies plotted, the largest amplitude peaks occur at the third-, fifth-, and seventh-order harmonics. For the $\ell/d = 0.5$ case, there are prominent amplitude spikes at the second- and fourth-order harmonics. The final three cases closely resemble the stationary cylinder and oscillating $\ell/d = 0$ case, with the main difference being the amplitudes. These trends are in agreement with the lift history plots, as the waveform transition cases ($\ell/d = 0.25$ and $\ell/d = 0.5$) have additional frequency content that indicate unsteadiness not associated with the $\ell/d = 0$ or $\ell/d \geq 0.75$ cases.

The trends in the FFT plots can be associated with the mechanisms dictating the flowfield. The interaction of shear layer roll-up with edge vortex formation occurs in cases that exhibit additional frequency spikes in their FFT plots. It can be concluded that the complexity in vortex formation and detachment causes variability in the forces seen by the disturbance generator. Additional frequency spikes in the FFTs do not occur for cases where the splitter plate is either absent, or is long enough to be the primary source of vortex formation and detachment. The lack of a splitter plate, and therefore an edge vortex, means that shear layer interaction is the only cause of vortex formation of both stationary and rotating cylinders. For cases with splitter plates attached, consistent vortex shedding is achievable by preventing the shear layers from having a significant influence on the edge vortex formation.

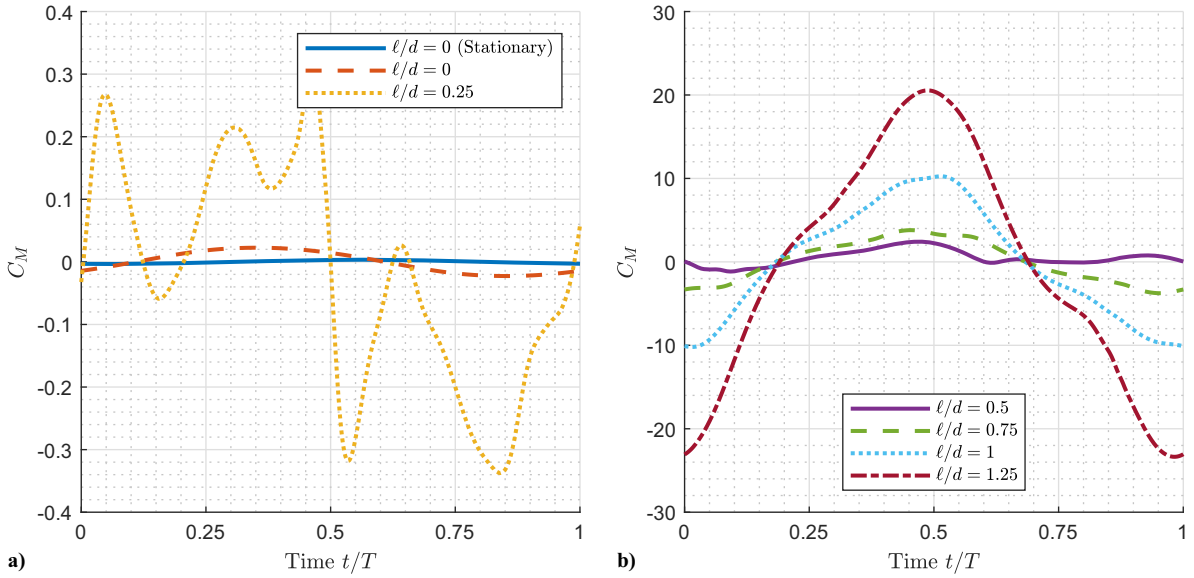

Fig. 15 Pitching moment coefficient plots for a complete cycle: a) $\ell/d = 0$ (stationary), $\ell/d = 0$, and $\ell/d = 0.25$; b) $\ell/d = 0.5$, $\ell/d = 0.75$, $\ell/d = 1$, and $\ell/d = 1.25$.

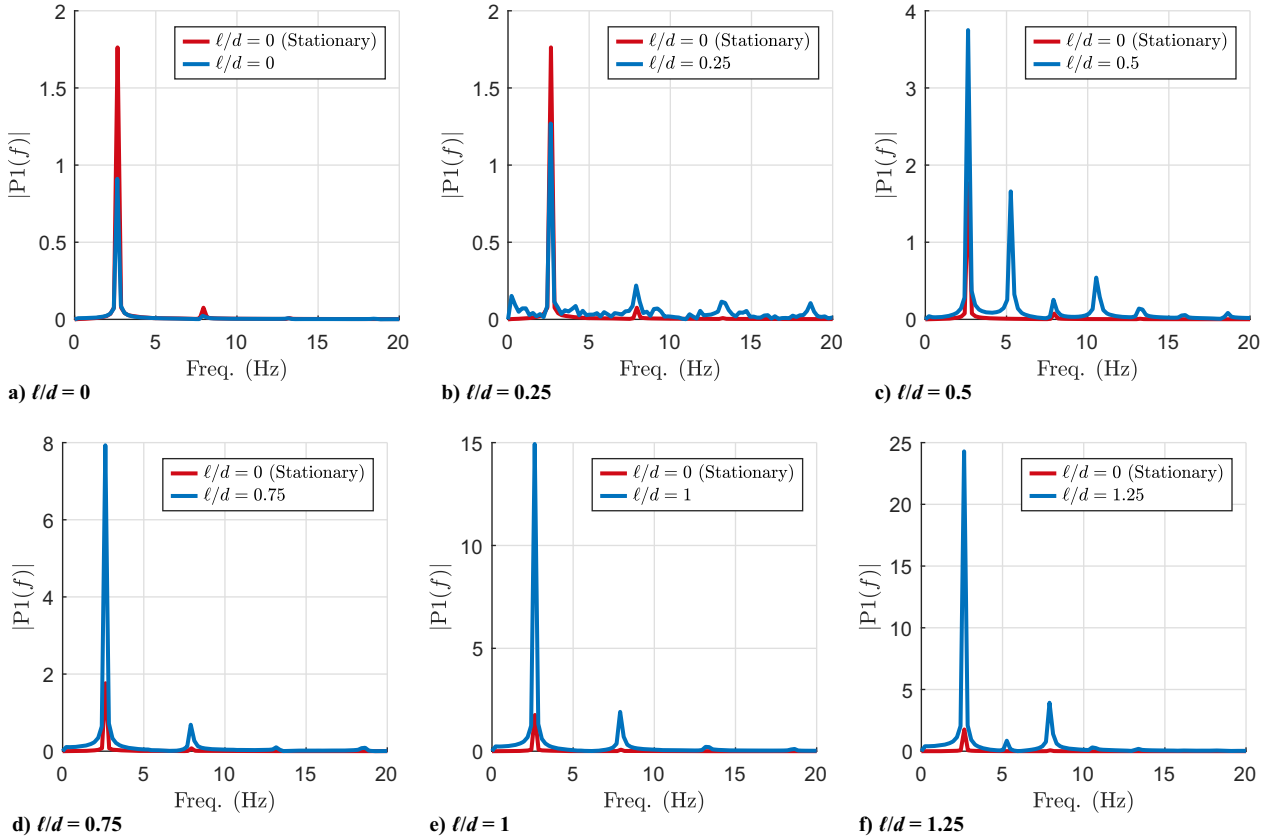

Fig. 16 FFT plots of lift coefficient for the various geometries.

C. Far Wake

The far wake exhibits some interesting features that will impact a downstream body experiencing the velocity and flow-angle fluctuations generated by the disturbance generator. Figure 17 shows the cycle-averaged streamwise velocity profiles for the various geometries at different downstream distances ranging from $x/d = 2$ to $x/d = 8$. Starting with the case of $\ell/d = 0$, the velocity profile at $x/d = 2$ shows a large velocity deficit compared to the next downstream location. The wake deficit gradually decreases with increasing downstream distance. For the case of $\ell/d = 0.25$, larger velocity deficits can be noticed at all the locations. Similar to the $\ell/d = 0$ case, the deficit region progressively diminishes with increasing x/d. This is also the first case where very small signs of asymmetry are present, as evident one diameter below the flow centerline at $x/d = 2$. This deviation is too minor to be noticed in the previously discussed wake contours. In addition, small regions of velocity surplus begin to appear in the wake at this location. The half-diameter case shows clear asymmetry, and a majority of the wake appears to be a deficit region. The case of $\ell/d = 0.75$ is the first occurrence of prominent velocity surplus regions in the center of the wake. Moving downstream from $x/d = 2$, the surplus consistently decreases until a deficit is again reached at $x/d = 8$. The wake is fairly symmetric over a full cycle. Finally, the cases of $\ell/d = 1$ and $\ell/d = 1.25$ give the largest surplus along the flow centerline at all the downstream locations. The wake is largely symmetric for $\ell/d = 1$ and $\ell/d = 1.25$, with the latter case showing a small amount of asymmetry in the y variation of the streamwise velocity, i.e., a shift away from the flow centerline at locations further downstream.

In summary, some of the velocity profiles display large areas around the flow centerline with either a velocity surplus or deficit. The regions away from the flow centerline, however, do not always follow the same trend. Moreover, a consistent pattern does not exist with increasing plate length in terms of asymmetry and the intensity of the velocity deficit/surplus at a given point in the wake. Integrated velocities can be used to get a better idea of the overall wake behavior. The variation of normalized integrated velocity along the flow direction, shown in Fig. 18, helps to determine if the wake at a particular x/d location is overall a surplus or deficit and how this characteristic varies in the flow direction. For any particular splitter plate length, this velocity is calculated at each reported downstream x/d by taking the integral of the streamwise velocity difference, $(u - U_\infty)/U_\infty$, along the horizontal rake location extending from $y/d = -3$ to $y/d = 3$.

For the stationary cylinder, the velocity deficit in the wake increases in the flow direction. The oscillating cases of $\ell/d = 0$ and $\ell/d = 0.25$ do not display much variation in velocity deficit with downstream distance. That is to say that the average velocity in the wake does not change much within the distances tested. The difference in integrated velocity deficits for the first three cases (stationary $\ell/d = 0$, oscillating $\ell/d = 0$, and oscillating $\ell/d = 0.25$) are minimal, especially in regions close to the cylinder, from $x/d = 2$ to $x/d = 5$. Approaching a half-diameter plate length causes a noticeable increase velocity deficit in this region. For the case of $\ell/d = 0.5$, a larger variation in the integrated velocity occurs at all locations compared to the first two cases. The integrated velocity deficit actually shows a trend similar to the stationary cylinder, although the velocity deficit at every location is more negative. Interestingly, increasing the splitter plate length past $\ell/d = 0.5$ causes a sudden jump in this pattern owing to the sudden changes in the vortex shedding, and the nature of the wake shifts toward a velocity-surplus-producing tendency at all locations. Once the splitter plate length is increased to $\ell/d = 0.75$, the integrated velocity deficit at every downstream location begins to become less negative or, in other words, transforms into a velocity surplus relative to the previous cases. The cases of $\ell/d = 0.75$ and $\ell/d = 1$ still have integrated velocity deficit values that become more negative with increasing downstream distance, but they are much closer to having velocity surplus than all the previous cases. Of all the splitter plate lengths tested, only the plate length of $\ell/d = 1.25$ has a positive integrated velocity area at every downstream distance. This case also maintains a somewhat constant velocity surplus area for more distance downstream, only falling off after $x/d = 6$ is reached. It is interesting to note that the mean drag is positive for this case despite the velocity surplus at all locations in the wake. However, it should be

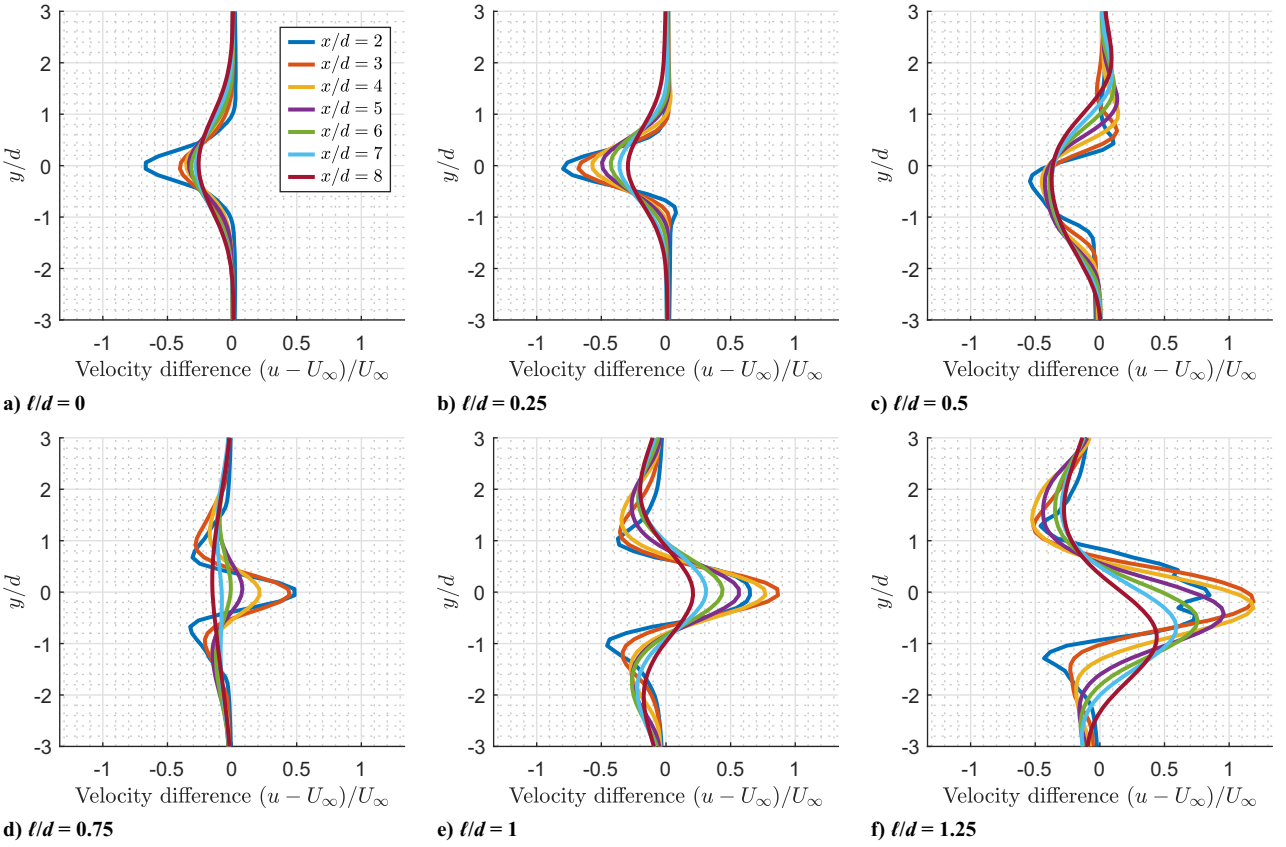

Fig. 17 Cycle-averaged mean streamwise velocities at downstream locations.

noted that the velocity deficit or surplus in the wake is only one of the contributions to the streamwise force in unsteady flows, and the nature of the force is also determined by other unsteady contributions from pressure and momentum flux [35,39–41].

The trends in the flow-angle fluctuations in the wake were also investigated using the effective angle of attack α_{eff} which is obtained as $\tan^{-1}(v/u)$ using the velocity data. Figure 19 shows the effective angle of attack FFTs for the various splitter plate lengths at a downstream location of $x/d = 5$. The effective angle of attack FFT for the stationary cylinder is largely similar to the lift coefficient FFT, with the primary frequency being that of the oscillation frequency, 2.65 Hz. Every splitter plate length chosen displayed this dominant frequency. Similar to the lift-coefficient FFTs, we see that the cases of $\ell/d = 0.25$ and $\ell/d = 0.5$ have frequency spikes at varying-order harmonics, while the final three splitter plate length cases have minimal irregularities. The correlation between the force FFTs and α_{eff} FFTs suggest that information regarding consistent vortex shedding and flow angle fluctuations in the wake may possibly be identified from the forces measurements on the cylinders alone in the absence of flowfield data.

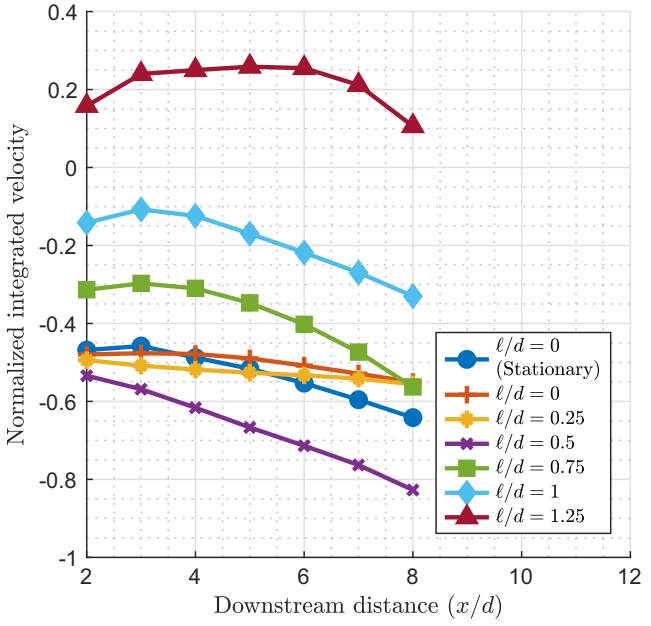

Fig. 18 Normalized integrated streamwise velocities at downstream locations.

IV. Conclusions

The unsteady flow pattern and the associated loads of several rotating geometries were numerically studied using an unsteady RANS CFD approach. Comparisons between a classic stationary circular cylinder, an oscillating circular cylinder, as well as five oscillating cylinders with attached splitter plates of varying length were discussed. Oscillating cases were sinusoidally oscillated to amplitudes of $\pi/4$ at the natural shedding frequency of the stationary cylinder. The shear-layer interaction mechanism and the vortex shedding pattern were analyzed using the flowfield data. The unsteady loads experienced by the geometries were studied using the lift, drag, and pitching moment coefficients. Further, velocity and flow angle fluctuations in the far wake were analyzed using the cycle-averaged mean velocities at several downstream locations.

Varying the splitter plate length resulted in several interesting wake patterns. The wake was found to be asymmetric for the case of $\ell/d = 0.5$, whereas it was symmetric for the shorter plate length case. This was the only case with a predominantly asymmetric wake, and this phenomenon coincided with the wake having the largest amount of velocity deficit. The wake asymmetry was found to be dependent on the initial rotation direction. For larger plate lengths, the trend toward a velocity surplus dominated wake increases rapidly. Analysis of the load-history FFTs along with the wake pattern suggested that the load signals can be a good indicator of wake

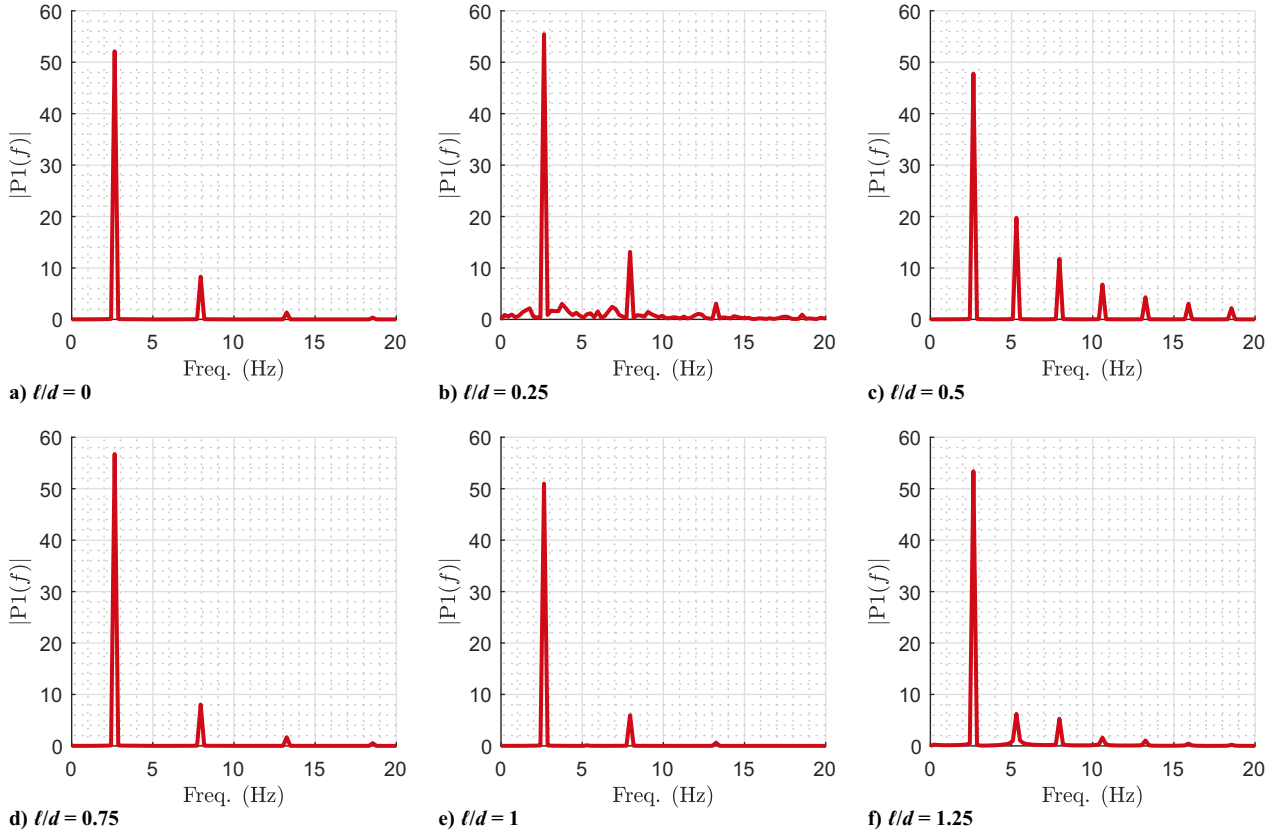

Fig. 19 Effective angle of attack FFTs at $x/d = 5$.

coherency in the absence of flowfield data. The frequency spikes in the FFTs were found to be primarily caused by the influence of shear layer roll-up on edge vortex formation. Cases in which the shear layers did not feed the edge vortex resulted in clean FFTs. Multiple frequency spikes in the C_L FFTs were observed in the $\ell/d = 0.25$ and $\ell/d = 0.5$ cases. These two cases demonstrated a transition period wherein the periodic lift curves had waveforms that were neither sinusoidal nor triangular. Increasing the splitter plate length to or above $\ell/d = 0.75$ reduced and eventually eliminated the additional harmonics in both the lift coefficient FFTs and effective angle of attack FFTs.

The current results suggest that the addition of a splitter plate on oscillating cylinders should employ plates that are long enough to prevent the interaction of rolled-up shear layers with same-signed edge vortices if the objective is to produce coherent vortical wakes. While the present research gives positive insight into the wake produced by cylinders with various splitter plate lengths, it is desirable to generate a broader map of the flow mechanisms surrounding disturbance generators of this type. Future efforts should incorporate different pitch amplitudes, and possibly various oscillation frequencies apart from the natural shedding frequency so that a broader case range may be explored.

Acknowledgments

The authors gratefully acknowledge funding support for this research from the National Science Foundation under Award No. CMMI-2015983 and program officer Robert Landers. The authors also acknowledge the computing resources provided by North Carolina State University High Performance Computing Services Core Facility (RRID:SCR_022168).

References

[1] Gong, W. Q., Jia, B. B., and Xi, G., "Experimental Study on Mean Thrust of Two Plunging Wings in Tandem," *AIAA Journal*, Vol. 53, No. 6, 2015, pp. 1693–1705. https://doi.org/10.2514/1.J053452

[2] Lefebvre, J. N., and Jones, A. R., "Experimental Investigation of Airfoil Performance in the Wake of a Circular Cylinder," *AIAA Journal*, Vol. 57, No. 7, 2019, pp. 2808–2818. https://doi.org/10.2514/1.J057468

[3] Kirschmeier, B. A., Gianikos, Z., Gopalarathnam, A., and Bryant, M., "Amplitude Annihilation in Wake-Influenced Aeroelastic Limit-Cycle Oscillations," *AIAA Journal*, Vol. 58, No. 9, 2020, pp. 4117–4127. https://doi.org/10.2514/1.J058942

[4] Biler, H., Badrya, C., and Jones, A. R., "Experimental and Computational Investigation of Transverse Gust Encounters," *AIAA Journal*, Vol. 57, No. 11, 2019, pp. 4608–4622. https://doi.org/10.2514/1.J057646

[5] Badrya, C., Biler, H., Jones, A. R., and Baeder, J. D., "Effect of Gust Width on Flat-Plate Response in Large Transverse Gust," *AIAA Journal*, Vol. 59, No. 1, 2020, pp. 49–64. https://doi.org/10.2514/1.J059678

[6] Badrya, C., Jones, A. R., and Baeder, J. D., "Unsteady Aerodynamic Response of a Flat Plate Encountering Large-Amplitude Sharp-Edged Gust," *AIAA Journal*, Vol. 60, No. 3, 2021, pp. 1549–1564. https://doi.org/10.2514/1.J060683

[7] Rockwood, M., and Medina, A., "Controlled Generation of Periodic Vortical Gusts by the Rotational Oscillation of a Circular Cylinder and Attached Plate," *Experiments in Fluids*, Vol. 61, No. 2, 2020, pp. 1–13. https://doi.org/10.1007/s00348-020-2882-3

[8] Williamson, C. H. K., "Vortex Dynamics in the Cylinder Wake," *Annual Review of Fluid Mechanics*, Vol. 28, No. 1, 1996, pp. 477–539. https://doi.org/10.1146/annurev.fl.28.010196.002401

[9] Rockwood, M. P., Taira, K., and Green, M. A., "Detecting Vortex Formation and Shedding in Cylinder Wakes Using Lagrangian Coherent Structures," *AIAA Journal*, Vol. 55, No. 1, 2017, pp. 15–23. https://doi.org/10.2514/1.J055051

[10] Okajima, A., "Strouhal Numbers of Rectangular Cylinders," *Journal of Fluid Mechanics*, Vol. 123, Oct. 1982, pp. 379–398. https://doi.org/10.1017/S0022112082003115

[11] Shao, C. P., and Wei, Q. D., "Control of Vortex Shedding from a Square Cylinder," *AIAA Journal*, Vol. 46, No. 2, 2008, pp. 397–407. https://doi.org/10.2514/1.28367

[12] Yogeswaran, V., Sen, S., and Mittal, S., "Free Vibrations of an Elliptic Cylinder at Low Reynolds Numbers," *Journal of Fluids and Structures*, Vol. 51, Nov. 2014, pp. 55–67. https://doi.org/10.1016/j.jfluidstructs.2014.07.012

[13] Liao, Q., Dong, G. J., and Lu, X. Y., "Vortex Formation and Force Characteristics of a Foil in the Wake of a Circular Cylinder," *Journal of Fluids and Structures*, Vol. 19, No. 4, 2004, pp. 491–510. https://doi.org/10.1016/j.jfluidstructs.2004.03.001

[14] Gehlert, P., and Babinsky, H., "Boundary Layer Vortex Sheet Evolution Around an Accelerating and Rotating Cylinder," *Journal of Fluid Mechanics*, Vol. 915, May 2021, Paper A50. https://doi.org/10.1017/jfm.2021.121

[15] Kimura, T., Tsutahara, M., and Wang, Z.-Y., "Wake of a Rotating Circular Cylinder," *AIAA Journal*, Vol. 30, No. 2, 1992, pp. 555–556. https://doi.org/10.2514/3.10953

[16] Tokumaru, P. T., and Dimotakis, P. E., "Rotary Oscillation Control of a Cylinder Wake," *Journal of Fluid Mechanics*, Vol. 224, March 1991, pp. 77–90. https://doi.org/10.1017/S0022112091001659

[17] Fujisawa, N., Ikemoto, K., and Nagaya, K., "Vortex Shedding Resonance from a Rotationally Oscillating Cylinder," *Journal of Fluids and Structures*, Vol. 12, No. 8, 1998, pp. 1041–1053. https://doi.org/10.1006/jfls.1998.0178

[18] Thiria, B., Goujon-Durand, S., and Wesfreid, J. E., "The Wake of a Cylinder Performing Rotary Oscillations," *Journal of Fluid Mechanics*, Vol. 560, Aug. 2006, pp. 123–147. https://doi.org/10.1017/S0022112006000656

[19] Lu, X.-Y., and Sato, J., "A Numerical Study of Flow Past a Rotationally Oscillating Circular Cylinder," *Journal of Fluids and Structures*, Vol. 10, No. 8, 1996, pp. 829–849. https://doi.org/10.1006/jfls.1996.0055

[20] Suresh Babu, A., Medina, A., Rockwood, M., Bryant, M., and Gopalarathnam, A., "Theoretical and Experimental Investigation of an Unsteady Airfoil in the Presence of External Flow Disturbances," *Journal of Fluid Mechanics*, Vol. 921, Aug. 2021, Paper A21. https://doi.org/10.1017/jfm.2021.484

[21] Cimbala, J. M., and Garg, S., "Flow in the Wake of a Freely Rotatable Cylinder with Splitter Plate," *AIAA Journal*, Vol. 29, No. 6, 1991, pp. 1001–1003. https://doi.org/10.2514/3.10692

[22] Hasan, M. A. Z., and Budair, M. O., "Role of Splitter Plates in Modifying Cylinder Wake Flows," *AIAA Journal*, Vol. 32, No. 10, 1994, pp. 1992–1998. https://doi.org/10.2514/3.12243

[23] You, D., Choi, H., Choi, M.-R., and Kang, S.-H., "Control of Flow-Induced Noise Behind a Circular Cylinder Using Splitter Plates," *AIAA Journal*, Vol. 36, No. 11, 1998, pp. 1961–1967. https://doi.org/10.2514/2.322

[24] Mansingh, V., and Oosthuizen, P. H., "Effects of Splitter Plates on the Wake Flow Behind a Bluff Body," *AIAA Journal*, Vol. 28, No. 5, 1990, pp. 778–783. https://doi.org/10.2514/3.25119

[25] Chatterjee, P., Jenkins, M., Suresh Babu, A., Medina, A., Gopalarathnam, A., and Bryant, M., "Tailored Bluff Body Motion for Generating Desired Wake Structures," *AIAA Aviation Forum*, AIAA Paper 2020-3007, 2020. https://doi.org/10.2514/6.2020-3007

[26] Hughes, M. T., Gopalarathnam, A., and Bryant, M., "Modulation and Annihilation of Aeroelastic Limit-Cycle Oscillations Using a Variable-Frequency Disturbance Generator," *AIAA Journal*, Vol. 61, No. 4, 2023, pp. 1447–1461. https://doi.org/10.2514/1.J062295

[27] Stringer, R. M., Zang, J., and Hillis, A. J., "Unsteady RANS Computations of Flow Around a Circular Cylinder for a Wide Range of Reynolds Numbers," *Ocean Engineering*, Vol. 87, Sept. 2014, pp. 1–9. https://doi.org/10.1016/j.oceaneng.2014.04.017

[28] Celik, I. B., Ghia, U., Roache, P. J., Freitas, C. J., Coleman, H., and Raad, P. E., "Procedure for Estimation and Reporting of Uncertainty due to Discretization in CFD Applications," *Journal of Fluids Engineering*, Vol. 130, No. 7, 2008, Paper 078001. https://doi.org/10.1115/1.2960953

[29] Rahman, M., Karim, M., and Alim, M. A., "Numerical Investigation of Unsteady Flow Past a Circular Cylinder Using 2-D Finite Volume Method," *Journal of Naval Architecture and Marine Engineering*, Vol. 4, No. 1, 2008, pp. 27–42. https://doi.org/10.3329/jname.v4i1.914

[30] Bardina, J., Huang, P., and Coakley, T., "Turbulence Modeling Validation, Testing, and Development," NASA TM-110446, 1997.

[31] Rosetti, G. F., Vaz, G., and Fujarra, A. L. C., "URANS Calculations for Smooth Circular Cylinder Flow in a Wide Range of Reynolds Numbers: Solution Verification and Validation," *Journal of Fluids Engineering*, Vol. 134, No. 12, 2012, Paper 121103. https://doi.org/10.1115/1.4007571

[32] Schlichting (Deceased), H., and Gersten, K., *Fundamentals of Boundary–Layer Theory*, Boundary-Layer Theory, Springer, Berlin, 2016, pp. 29–49.

[33] Aljure, D. E., Rodríguez, I., Lehmkuhl, O., Pérez-Segarra, C. D., and Oliva, A., "Influence of Rotation on the Flow over a Cylinder at Re = 5000," *International Journal of Heat and Fluid Flow*, Vol. 55, Oct. 2015, pp. 76–90. https://doi.org/10.1016/j.ijheatfluidflow.2015.07.015

[34] Williamson, C. H. K., "The Natural and Forced Formation of Spot-Like 'Vortex Dislocations' in the Transition of a Wake," *Journal of Fluid Mechanics*, Vol. 243, Oct. 1992, pp. 393–441. https://doi.org/10.1017/S0022112092002763

[35] Sunil, P., Kumar, S., and Poddar, K., "Flow Past a Rotationally Oscillating Cylinder with an Attached Flexible Filament," *Journal of Fluid Mechanics*, Vol. 930, Jan. 2022, Paper A3. https://doi.org/10.1017/jfm.2021.894

[36] Godoy-Diana, R., Aider, J.-L., and Wesfreid, J. E., "Transitions in the Wake of a Flapping Foil," *Physical Review E: Statistical, Nonlinear, and Soft Matter Physics*, Vol. 77, No. 1, Pt 2, 2008, Paper 016308. https://doi.org/10.1103/PhysRevE.77.016308

[37] Das, A., Shukla, R. K., and Govardhan, R. N., "Existence of a Sharp Transition in the Peak Propulsive Efficiency of a Low- *Re* Pitching Foil," *Journal of Fluid Mechanics*, Vol. 800, Aug. 2016, pp. 307–326. https://doi.org/10.1017/jfm.2016.399

[38] Cheng, M., Liu, G., and Lam, K., "Numerical Simulation of Flow Past a Rotationally Oscillating Cylinder," *Computers and Fluids*, Vol. 30, No. 3, 2001, pp. 365–392. https://doi.org/10.1016/S0045-7930(00)00012-8

[39] Ramamurti, R., and Sandberg, W., "Simulation of Flow About Flapping Airfoils Using Finite Element Incompressible Flow Solver," *AIAA Journal*, Vol. 39, No. 2, 2001, pp. 253–260. https://doi.org/10.2514/2.1320

[40] Bohl, D. G., and Koochesfahani, M. M., "MTV Measurements of the Vortical Field in the Wake of an Airfoil Oscillating at High Reduced Frequency," *Journal of Fluid Mechanics*, Vol. 620, Feb. 2009, pp. 63–88. https://doi.org/10.1017/S0022112008004734

[41] Shinde, S. Y., and Arakeri, J. H., "Physics of Unsteady Thrust and Flow Generation by a Flexible Surface Flapping in the Absence of a Free Stream," *Proceedings of the Royal Society A: Mathematical, Physical and Engineering Sciences*, Vol. 474, No. 2218, 2018, Paper 20180519. https://doi.org/10.1098/rspa.2018.0519

J. Larsson
Associate Editor